Dynamics of intrusion in downslope gravity currents in a rotating frame

Axel Tassigny,* Maria Eletta Negretti, and Achim Wirth
Univ. Grenoble Alpes, CNRS, Grenoble INP, LEGI, 38000, Grenoble, France

(Received 11 January 2024; accepted 3 June 2024; published 15 July 2024)

Gravity currents are ubiquitous in polar regions and marginal seas and play a crucial role in the formation of deep waters in the ocean. They contribute to the vorticity and energy transfers towards the ocean interior. We present results from an experimental study on downslope intruding gravity currents into an initially two-layer stably stratified ambient on a rotating platform at high buoyancy Reynolds numbers. We identify a turbulent process for the downslope transport, intermittent and localized, which takes the form of cascading. This process is intrinsic to rotating gravity currents, i.e., it arises without any external tuning, and the related transport does not exhibit any characteristic length scale, suggesting self-organized criticality. The cascading intrusion mechanism reveal to be the main contributor to the vorticity and turbulence in the ambient interior, with a dependence on the Coriolis parameter f and the density anomaly to the surrounding ambient. Two mechanisms for vorticity production are recognized: first, the spreading of the intrusion from cascading into the interior and, second, the meandering and breakup of the deep boundary current (formed from downward Ekman transport) induced by intrusion from cascading. When the intrusion spreads at the pycnocline only, anticyclonic eddies are formed in the intrusion and top layers, whereas for intrusions spreading through the full bottom layer, vortices of both signs are generated due to bottom friction. The turbulence in the receiving ambient reveals to be horizontally isotropic, nonstationary, and nonhomogeneous. Energy is injected through the intrusion issued by cascading at the penetration length scale L_p and forces the turbulence in the intrusion area close to the slope. The central area far from the boundaries is characterised, instead, by freely evolving two-dimensional turbulence, forced at large scales. These results suggest a complementary way to interpret oceanic observations of gravity currents spreading in the ocean interior.

DOI: 10.1103/PhysRevFluids.9.074605

I. INTRODUCTION

Predicting the response to natural and anthropogenic forcings of the Earth's climate is one of today's greatest challenges. It crucially depends on our understanding of the ocean dynamics over a large variety of interacting scales in time and space. Water mass generation and mixing is one important mechanism that drives the energy balance in the ocean and is related to turbulent submesoscale processes that are still poorly understood.

The abyssal waters are mainly fed by oceanic overflows, or gravity currents, originating from accumulation of dense water by convection on continental shelves [1] or from dense water outflows of marginal seas [2]. The dense water masses follow then the bottom topography driven by gravity and are influenced by the Earh's rotation, which makes them deviate to the right (left) in the northern (southern) hemisphere, a process known as geostrophic adjustment. Several papers [3–14] attempt to give conceptual models to describe such currents in a rotating frame. The importance of geostrophic balance in the case of downslope gravity currents in the Weddel Sea was raised first in 1973 by Gill

*Contact author: axel.tassigny@univ-grenoble-alpes.fr

[15]. A well-established scheme was proposed by Shapiro and Hill [10] (see also [11]), where the gravity current is geostrophically adjusted along slope within one rotational day, while part of this dense water mass is transported downslope due to friction. Stream-tube models followed [16,17], in which it is assumed that the physical properties vary in the streamwise (along slope) direction of the gravity current only, and cross-stream variations are integrated in the across slope direction. The geostrophic adjustment of gravity currents has also shown to produce vortices in the above surface layer under certain conditions [4–7,18–21] or geostrophic eddies due to abrupt topography changes, such as the meddies from the Mediterranean outflow in the Gulf of Cadiz [22]. Later, theoretical studies [4,8,9,23] suggested considering the rotating gravity current as composed of two interacting parts: the main flow, the "vein," geostrophically adjusted moving along slope at the geostrophic velocity [3], and a friction layer, characterized in some regimes by roll waves [4], in which the geostrophic balance is perturbed by friction, nonlinearity, and turbulent fluxes; herein, part of the water mass escapes the vein and flows downslope, a phenomenon which may be enhanced by the presence of canyons in the bathymetry [24,25]. Negretti, Tucciarone, and Wirth [19] confirmed this gravity current dual structure on the slope area by temporal averages of velocity measurements throughout the experimental duration ($\approx$150 rotational days) and characterized the global circulation (see also [26]) induced in the ambient interior for different intrusion types, including bottom (nonintruding) gravity currents.

All these approaches are based on a continuous downslope evolution of the gravity current. This concept is challenged in the present study: we show that the intrusion from a gravity current into the receiving ambient in a rotating frame is not a continuous process of the main vein, but happens through highly energetic, intermittent, and localized discharges of saline water escaping from the vein, complementary to the friction layer, which we call *cascading*, which exhibits a fractal behavior. The intrusion is hence not just a tongue of saline water with front (shear) instabilities, but a combination of unstable density fronts, filaments, loops of higher velocities from detached deep boundary currents, and vortices of different size issued by the intrusion process itself and in mutual interaction, which propagate into the interior. This rich intrusion provides hence a large variety of interacting processes that drive turbulence, turbulent mixing, energy transfer, and dissipation over an extended variety of scales in space and time. As discussed by Wells, Cenedese, and Caulfield [27], this is important since the resulting mixing influences the density, the final stabilization depth of the water mass, and its (dyapicnal) transport in the world's oceans [28–30]. On a local scale, gravity currents' intrusion processes have shown to produce interannual to decadal ocean variability [31].

The focus of this paper is on the dynamics of the intrusion process and its statistical description, as well as on the characterization of the subsequent vorticity field and turbulence generated in the receiving ambient, using the high-quality and fine-scale dataset collected during the experimental campaign TUBE [19]. The turbulence induced by intruding gravity currents in a rotating frame as in those experiments [19] is closer to realistic ocean conditions and may produce different turbulence scenarios as compared to previous studies [32–41]. Indeed, it is unlikely that there is a single mechanism that dominates geophysical turbulence [42,43], and today's research aims at identifying the various possible dynamical processes, understanding their physics [44,45] and evaluating their impact [46–48].

Section II briefly describes the experimental set-up and define the relevant parameters. Section III focuses on the intrusion dynamics and in particular the new intrusion mechanism: cascading. The effects of this intrusion in the receiving ambient are quantified in Sec. IV in terms of vorticity and turbulence characteristics. Section V summarizes the results and gives concluding remarks.

II. EXPERIMENTAL SETUP AND FLOW SCALES

The experimental campaign TUBE, whose setup is sketched in Fig. 1 and described in detail elsewhere [19], has been performed in 2019 and 2021 over 4 months each, in the Coriolis Rotating Platform at LEGI (Grenoble, France). Essential details are recalled below.

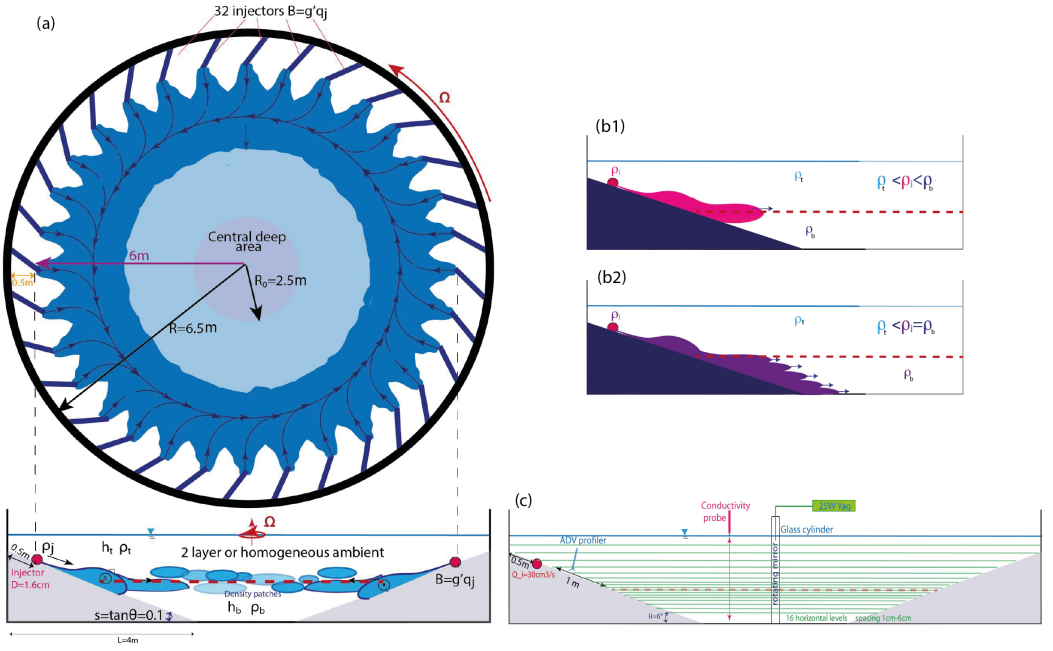

FIG. 1. (a) Schematic top and side view of the experimental design. $n = 32$ pipes positioned 50 cm from the tank edge and directed by 45°, injecting continuously saline solutions at a density of ρ_j at a constant flow rate ranging as $q_j = (32\text{–}43)$ cm^{3}s^{-1} into a two-layer stably stratified ambient. The axisymmetric conical slope has an inclination of 6° and a total length of 4 m. The central deep area has a diameter of 5 m. (b1–2) Sketch of the two cases considered. (b1) Intrusive cases with $\rho_t < \rho_j < \rho_b$ with a tongue of saline water intrusion at the pycnocline; (b2) bottom cases with $\rho_t < \rho_j = \rho_b$ and where the intrusion takes the form of fingers into the bottom layer. (c) Side view sketch of the measurements techniques used with 16 horizontal slices for the PIV measurements, along with the conductivity probe position mounted on a 1 m scanning axis to monitor the vertical density structure throughout the experiment.

The tank was initially filled with two homogeneous layers of different densities, ρ_t and ρ_b, with $\rho_b > \rho_t$ and had an anticlockwise (cyclonic) rotation expressed in terms of the Coriolis parameter $f = 4\pi/T$, where T is the rotation period of the tank. Saline solutions with density ρ_j were injected using a pump through 32 plexiglas tubes equally spaced on the Coriolis platform's circumference at $r = 6$ m and directed by 45° in the sense of rotation to help geostrophic adjustment on the top of an inclined boundary, shaped as an inverted cone with a circular cross section descending toward the center of the tank (cf. Fig. 1). The inclined boundary descended from the tank edge by 41 cm toward the center of the tank over a length of 4 m yielding a slope of $s = 0.1$, and leaving the portion of the tank within a radius of $R_0 = 2.5$ m from the center with a constant depth, hereafter called the "central deep area." The total injected flow rate $Q_{\text{inj}} = \sum_{j=1}^{n} q_j$, with $n = 32$ injection points, yielded an outlet injected velocity from the nozzles u_j larger than the Nof speed [3] $u_{\text{Nof}} = g's/f$ (cf. Table I), where $g' = g\Delta\rho/\rho_t$ is the reduced gravity, with $\Delta\rho = \rho_j - \rho_t$ and g is gravity. No water was discharged during the experiments. This particular experimental setup based on an axisymmetric configuration enables azimuthal averages allowing us to separate turbulent fluctuations from an average circulation even for a nonstationary flow. This allows us to follow the evolution of the turbulent field in the receiving ambient for a long duration (typically 150–220 rotational days), without imposing any characteristic length scale. The performed experiments along with their main characteristics are listed in Table I. Based on the relative values of ρ_j, ρ_t, and ρ_b, we consider two distinct sets of experiments that are depicted in Fig. 1(b): both are intrusive gravity

TABLE I. Experimental parameters and initial conditions, with the primary and derived parameters and the relevant nondimensional numbers.

Parameter	Exp05	Exp06	Exp07	Exp11	Exp09
h_t (cm)	37	37	38	40	38
h_b (cm)	17	16	16	14	16
H (cm)	6.3	5.5	5.8	5.2	14.2
g' (cm s^{-2})	5.5	5.1	5.1	5.5	12.75
f (s^{-1})	0.2	0.1	0.14	0.2	0.14
R_d (cm)	28	51	39	25	97
u_{Nof} (cm/s)	2.6	4.9	3.6	2.6	9.1
u_j (cm/s)	11.4	13.4	13.8	13.5	13.6
S	4.4	2.8	3.8	5.2	1.5
F_h	0.2	0.24	0.25	0.24	0.19
F_v	1.2	1.5	1.5	1.54	0.95
Ro	0.09	0.21	0.16	0.11	0.16
Re/10^5	6.8	8.0	8.2	8.1	8.1
$\mathscr{R}/10^4$	2.7	4.7	5.2	4.5	2.0
Bu/10^{-2}	1	5	3	1	7

currents, the former (b1) with an injected density between the top and bottom layers of the initial ambient, the latter with an intrusion density very close to the bottom layer.

The horizontal velocities were determined using the optical, nonintrusive experimental technique of particle image velocimetry (PIV), with a system allowing us to illuminate the full tank on 16 horizontal levels not equally spaced concentrated at the pycnocline level [cf. Fig. 1(c)]. The highest and lowest levels are at 51 cm and 7 cm from the bottom, respectively. Each element of the computed vector field from the PIV, with an acquisition frequency of 1 Hz, represents an area of roughly 0.5 cm × 0.5 cm. The time required to scan all 16 levels was 86.5 s. A 125 MicroScale Conductivity and Temperature Instrument (MSCTI, PME Vista, California) was employed to measure the electrical conductivity (and temperature) of the water in the central deep area at one horizontal location, installed at a distance of 1.08 m from the center of the tank [see Fig. 1(c)] mounted on a 1 m axis moving vertically throughout the full duration of the experiment with a velocity of 1 cm s^{-1} between $z = 1$ and 51 cm, every 60 s. The probe was calibrated at the beginning and at the end of each experiment. The density at the injection was constantly monitored by a fixed conductivity probe. Finally, flow visualization was realized using Rhodamine 6G at the injection to highlight the intruding current. The dye was injected at different times during the experiment, and a GoPro camera was equipped with an orange filter to separate the Rhodamine emitted spectrum from that of the PIV particles. Further details on the measurement techniques are given in Negretti *et al.* [19].

The parameters (primary and derived) are the slope s, the Coriolis parameter f, the difference between the injected density and the density of the top layer in the receiving ambient expressed in terms of the buoyant acceleration g', and the kinematic viscosity ν. The characteristic vertical scales are the depth of the bottom layer h_b and the intrusion thickness $H = \gamma h_b$, where $\gamma = (\rho_j - \rho_t)/(\rho_b - \rho_t)$, is a ratio of density differences and measures the portion of intruding water in the bottom layer. The characteristic horizontal scales are the typical size of the central deep area, here $L \equiv 600$ cm representing the diameter of the central area from the intrusion level, and the Rossby deformation radius $R_d = \sqrt{g'H}/f$. The characteristic velocity scales are the injection velocity u_j, which will be considered the reference velocity scale and the geostrophic velocity u_{Nof}, which ratio [19] $S = u_j/u_{\mathrm{Nof}}$ is a measure of the ratio between the geostrophic and the topographic slope.

The overall relevant nondimensional numbers are the horizontal and vertical Froude numbers $F_h = u_j/\sqrt{g'L}$, $F_v = u_j/\sqrt{g'h_b}$, respectively (where $F_h = F_v h_b/L$), the Rossby number $\mathrm{Ro} = u_j/(fL)$, the Reynolds number $\mathrm{Re} = u_j L/\nu$, the buoyancy Reynolds number $\mathscr{R} = \mathrm{Re}F_h^2$, and

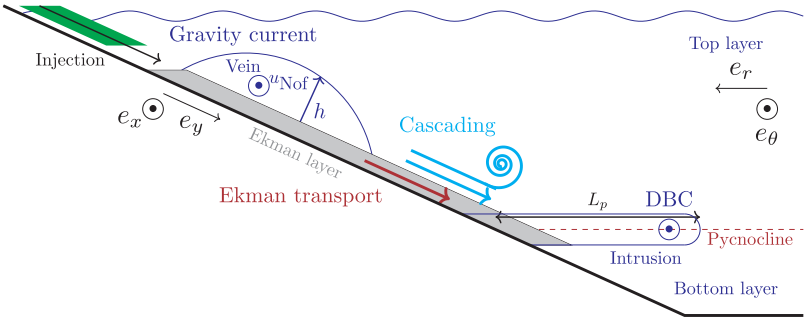

FIG. 2. Schematic description of the rotating gravity current on the slope, including the vein, the Ekman transport, the cascading, and the DBC.

the Burger number $\mathrm{Bu} = R_d^2/L^2$. The ratio f/N_0 gives the importance of rotation with respect to the stratification [38]. The values of these parameters for the considered experiments are reported in Table I.

In the following sections, some of the results are presented for two representative cases only, Exp07 for the intrusive gravity current and Exp09 for the bottom intrusive gravity current. They correspond to the sketch in Fig. 1, (b1) and (b2), respectively. Results from Exp05, Exp06, and Exp11 are qualitatively similar to Exp07.

III. DYNAMICS OF DOWNSLOPE TRANSPORT AND INTRUSION

A. Qualitative description

As outlined in Negretti *et al.* [19], once the saline solutions are injected, the flow is deviated to the right due to the Coriolis force and the structure of the gravity current is generated, with a thick vein overlaying a thin frictional layer [8,10,19]. A schematic view of the dynamics of the rotating gravity current is sketched in Fig. 2. In the spatiotemporal average, the gravity current is characterized by a main part, the vein, with an along slope velocity u_{Nof} and by the friction layer with a mainly downslope velocity [19], which generates due to an unbalance between the gravity force and the Coriolis force close to the bottom. This dynamics may be modified by topographic changes, such as canyons [25], or by ambient currents and/or different inflow conditions [10,11], processes not considered here. In this averaged configuration, when the dense water reaches the level of neutral buoyancy through the Ekman layer, a deep boundary current (DBC) forms, with the main velocity component being azimuthal. The horizontal penetration distance taken from the slope of the intrusion at the pycnocline, i.e., of the DBC, is of the order of $L_p = u_{\mathrm{Nof}}/(2f)$ [26,49], as depicted in Fig. 2. This is the first intrusion mechanism.

An important observation from the present experiments is the existence of another intrusion mechanism in which water from the gravity current on the slope (the vein) is discharged intermittently and locally, producing cascading (cf. Fig. 2). These discharges are produced spontaneously, i.e., with an initial quiescent receiving ambient and with a constantly and uniformly injected buoyancy flux. This intrusion mechanism is turbulent.

Figure 3 highlights these two intrusion mechanisms, using the combined dye (scalar) field tracing the injected fluid and the measured PIV field for experiment Exp07, at different times. The left column superposes the 10% larger norm's values of the velocity $||u||$, the middle column, the normalized vorticity field ζ/f and the right column, the radial velocity field u_r. At an early stage of the experiment (top panels), the DBC issued from the first intrusion mechanism remains attached to the slope boundary; it is highlighted by the bands of higher norm velocity (colormap) and high vorticity due to shear in the correspondent vorticity field (white dashed lines). A first intrusion through cascading is highlighted by a white arrow, appearing at $t/T = 68$, until $t/T = 72$. The

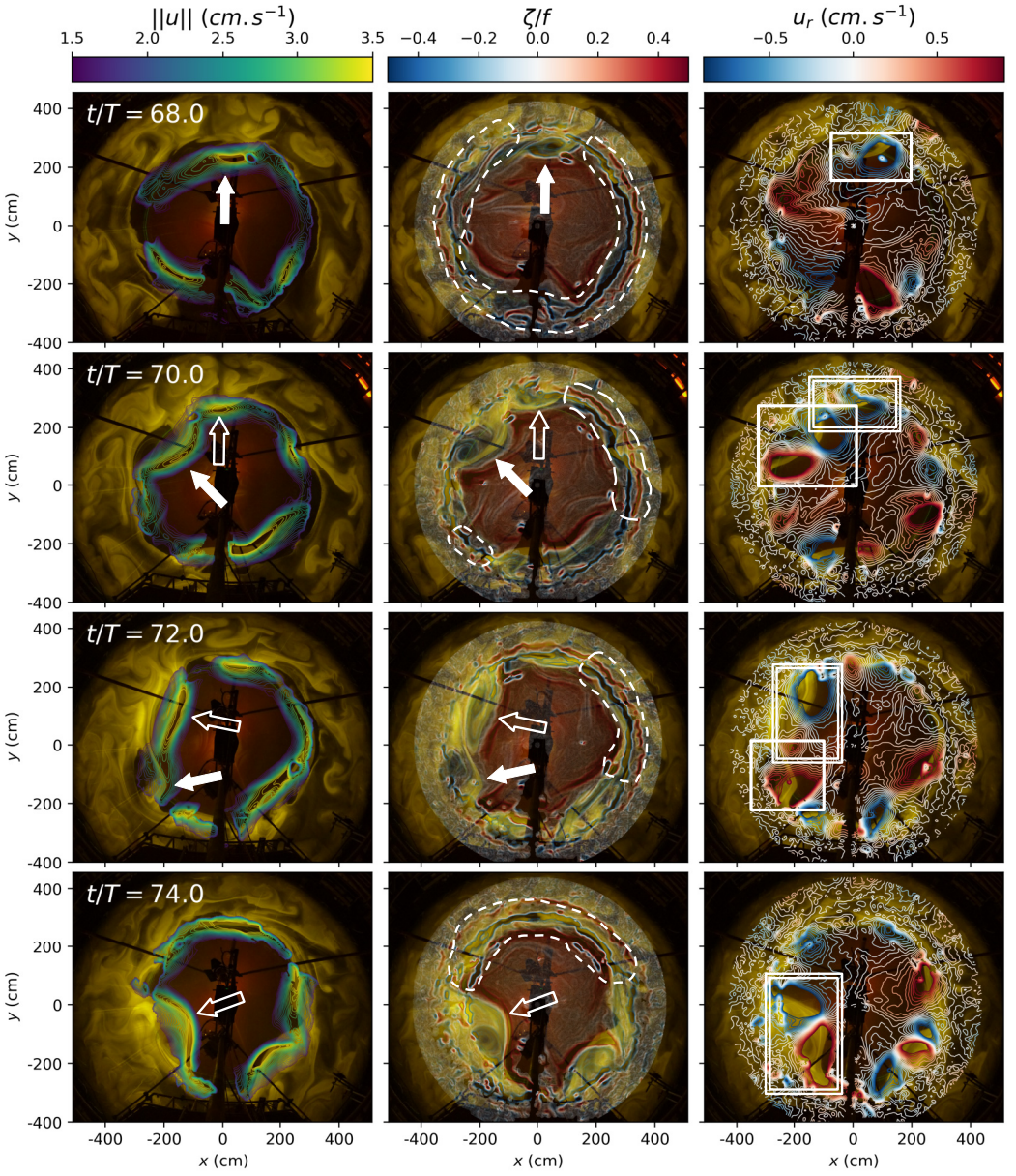

FIG. 3. Description of the intrusion mechanisms (the shear of the DBC: dashed lines, cascading: white arrows) in Exp07 at different times. Images of fluorescent dye injected in the saline inflow are superposed with the contour plot of the 10% larger norm's values of the velocity $||u||$ (left column), with the normalized vorticity field ζ/f (central columnn) and with the radial velocity field u_r (right column) at the pycnocline level ($z = 17.5$ cm). Two intrusions from cascading, propagating cyclonically into the boundary current, are clearly visible and marked with white arrows. The signature of the cascading intrusions in the radial velocity fields is highligthed by white squares in the right column, the first appearing in time filled, the second empty.

intruding water from cascading is then deviated to the right by the Coriolis force generating a core of negative vorticity that grows in (cf. the vorticity fields from $t/T = 70$ to $t/T = 74$). At the same time, the maximum norm velocity increases at the front of the intrusion, causing a local acceleration

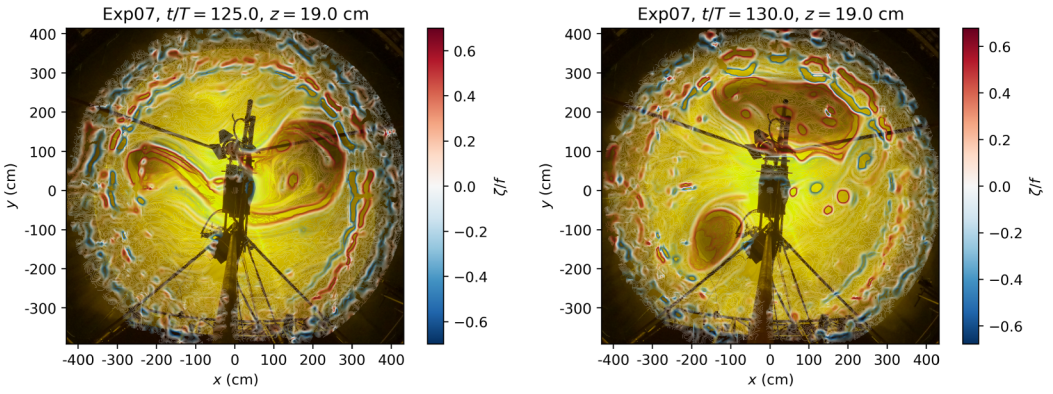

FIG. 4. Instantaneous vorticity field at the pycnocline level ($z = 19$ cm) for experiment Exp07, obtained from the measured PIV fields (red and blue) superposed on an instantaneous image of the scalar field with the injected fluid highlighted by fluorescent dye (yellow), at two different times [$t/T = 125$ (a), $t/T = 130$ (b)]. The closed loops of positive vorticity represent the reconnection of the broken original DBC pushed off-shore by cascading intrusions.

of the DBC (cf. left column). A second cascading is highlighted by an empty white arrow appearing at $t/T = 70$. The intrusion from cascading can also be recognized from the radial velocity fields: it exhibits a dipole with a negative and an adjacent positive radial velocity area, the first located upstream with respect to the second in the DBC (see white squares in the right column of Fig. 3). It is this second mechanism of intrusion, through cascading, which appears to be the dominant intrusion mechanism. A supplementary phenomenon is observed: when cascading events appear and reach the neutral buoyancy level, they push the original DBC off-shore, leading it to meander (see the deformation of the higher velocity bands in the left column of Fig. 3), which then eventually breaks on occasion into bands and loops of elevated speed with a positive vorticity core at later stages of the experiments, as shown in Fig. 4.

From these observations, it is evident that the intrusions from cascading are localized in space and intermittent in time. A detailed statistical description of this intrusion process is presented in the next section.

B. Cascading and self-organized criticality

The above observations suggest that the cascading process underlying the turbulent transport mechanism may obey a self-organized criticality (SOC), a concept developed in 1987 by Bak, Tang, and Wiesenfeld [50] to describe the behavior of complex systems with multiple degrees of freedom and a critical state, which is sensitive to small perturbations. The system is said *self-organized*, as it gets back to this critical state without any external tuning. This return to the critical state is done through intermittent and localized events (called avalanches or cascades) whose amplitude follows a power-law distribution [50] and has no characteristic scale and a fractal behavior [51]. This concept has been widely applied to many fields, from the stability of sand piles [50], to earthquakes, forest fires [52], and even knit elasticity [53]. In geophysical fluid dynamics, two pioneering papers revealed that this behavior is observed for Holmboe waves in stratified shear flows [54] and for the vertical overturning scales, characterizing an oceanic stratified shear flow [51]. In those studies, the critical parameter which determines the state of equilibrium is the Richardson number Ri, giving the ratio between the stabilizing effect of the stratification and the destabilizing effect of shear.

In our case, the injection velocity u_j exceeds the geostrophic velocity u_{Nof} that is fixed with the initial parameters (s, g', f, ν). This causes an anomaly of vorticity in the gravity current and will be discussed further below.

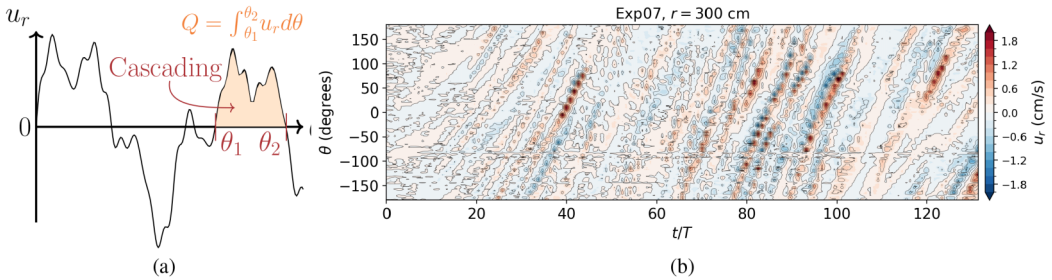

FIG. 5. (a) Sketch of the definition of intrusion from cascading using the radial velocity u_r. (b) Hovmöller diagram of the radial velocity for the radius $r_{\text{obs}} = 300\,\text{cm}$ for Exp07.

To detect an intrusion from cascading, we use the radial velocity field distribution close to the intrusion level, which marks the cascading with a dipole of positive and negative radial velocity as shown in the right column of Fig. 3. For a fixed radius $r_{\text{obs}} = 300\,\text{cm}$ at the level of the pycnocline, we define an intrusion from cascading as an interval where the function $\theta \longmapsto u_r(r_{\text{obs}}, \theta)$ has a positive sign, as depicted in Fig. 5(a). Similar results are also obtained using the negative radial velocities, since, as explained in the previous section, an intrusion through cascading produces a dipole of negative and positive radial velocity areas.

The temporal resolution of the experiments enables us to follow the development of an intrusion from cascading in time, as shown in the Hövmoller diagram in Fig. 5(b). Events of positive (blue) and negative (red) radial velocities are plotted over the full experimental duration at all θ and at the chosen radius r_{obs}. Clear bands can be identified whose inclination give a phase speed of roughly $2\,\text{cm}\,\text{s}^{-1}$, which scales with the advection velocity of the DBC. The Hovmöller diagram enables to define a lifetime of the intrusions.

In order to determine the lifetime of the intrusions from cascading, a specific correlation algorithm has been developed based on the superposition of the intervals (cf. Fig. 5) at two successive times. The detailed description of the method and its robustness is given in Appendix A.

Figure 6 displays the intrusion's duration from cascading τ, which follows a power-law distribution $PDF_\tau(t) \sim t^{-\mu}$ over more than one decade, from 1 to 20 rotational days. Note that only results

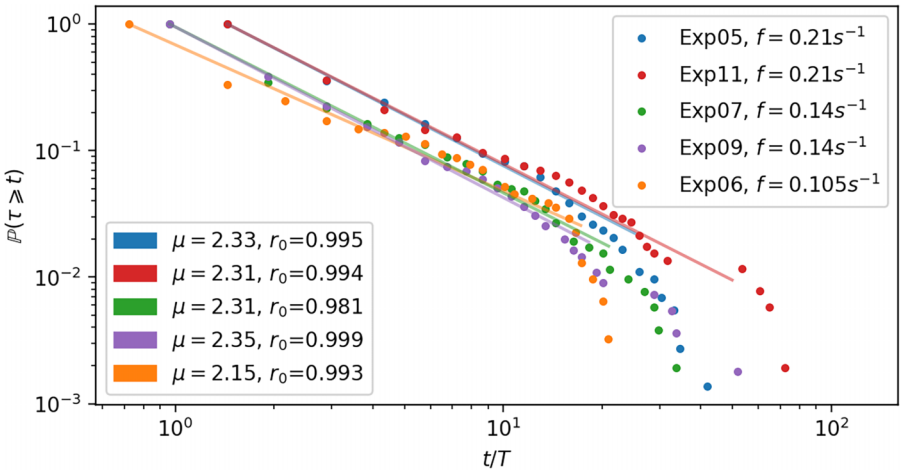

FIG. 6. Survival function of the lifetime of the cascading's intrusions $\mathbb{P}(\tau \geqslant t)$ for all considered experiments. The fractal dimension of the power law, μ, is computed with a linear regression of a log-log plot of the survival function of τ. r_0 is the coefficient of determination of the linear regression.

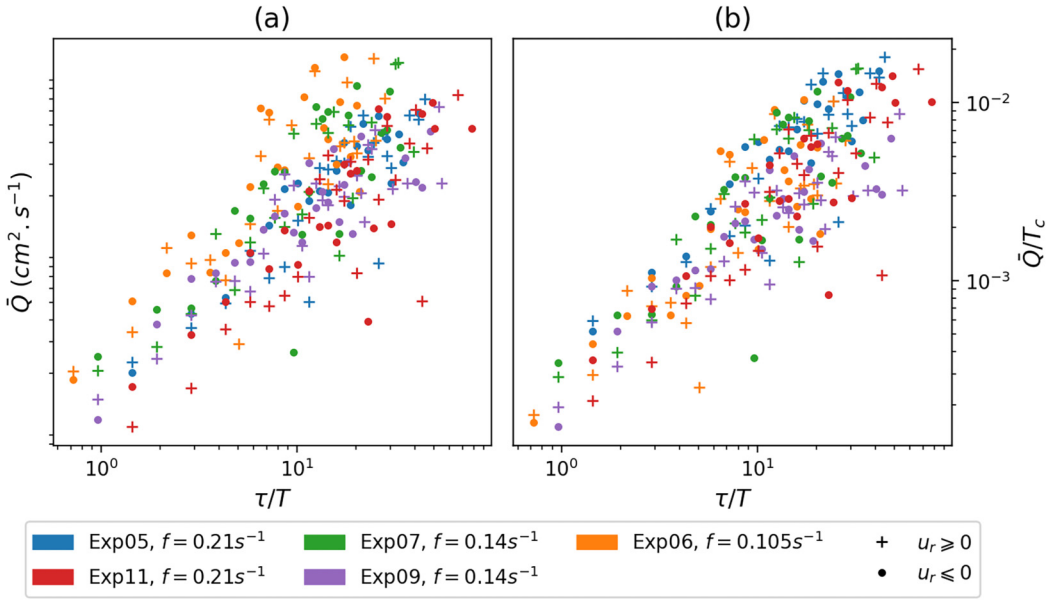

FIG. 7. Dimensional averaged transport $\bar{Q} = \langle Q \rangle_t$ over the lifetime of an intrusion from cascading τ/T (a) and after normalization with the Ekman transport $T_c = (\delta_{Ek} u_{\mathrm{Nof}}/2)[L/(h_b \gamma)]$ (b) for all considered experiments.

for positive velocities are presented. The fractal dimension of the power law, μ, is computed with a linear regression of a log-log plot of the survival function of τ, given by

$$\mathbb{P}(\tau \geqslant t) = \int_t^{+\infty} PDF_\tau(s)\, ds \propto t^{1-\mu}. \tag{1}$$

The survival function is preferred to the probability density function because its calculation does not require data sampling and is therefore less subject to noise. To avoid taking into account the tail cutoff, due to finite-size effects, the linear regression is weighted by $\mathbb{P}(\tau \geqslant t)^2$ to consider the larger sample size for lower t. The exponent μ is found to be between 2.1 and 2.3 varying slightly with the experiment but with no clear dependence on the experimental parameters. A slight dependence of μ with the observation radius r_{obs} and the correlation method is observed, but always falls into the range $2.1 < \mu < 2.6$. Values $\mu < 3$ imply that the lifetime distribution has no moment of order larger than one, and especially that it has an infinite variance. These results are in accord with the definition of SOC [51].

The transport (per unit thickness) by an intrusion from cascading into the ambient interior is estimated by

$$Q(t) = \int u_r(t) r\, d\theta. \tag{2}$$

The averaged transport $\bar{Q}$ over the lifetime of an event is correlated to the lifetime of the event τ as depicted in Fig. 7, where its conditional expectancy reveals to be proportional to a power of τ, i.e., $\langle \bar{Q} | \tau \rangle \propto \tau^\alpha$.

It may be expected that the transport of an intrusion from cascading is linearly proportional to its lifetime. However, Fig. 7(a) shows that the averaged transport is itself a function of τ since it grows with its lifetime. We also see that increasing the rotation rate reduces the transport $\bar{Q}$.

A scaling of the intrusion's transport can be deduced from the shallow-water equations governing the gravity current as proposed by Wirth [8] and Wåhlin and Walin [9]. Let us consider an inclined

plane of slope s with the vertical axis z perpendicular to the bottom, as depicted in Fig. 2. The x and y coordinates are defined along slope and across slope, respectively, with y pointing downslope toward the center of the tank. As described in Wirth [8], and as also depicted in Fig. 2, the rotating gravity current is composed of a vein with height h and a bottom friction layer. u and v are the vertically averaged velocities in the x and y directions, respectively. The inviscid stationary solution of the momentum conservation equation in the along-slope direction gives the geostrophic equilibrium

$$f u_0 = -g'(\partial_y h - s). \tag{3}$$

Averaging over the vein, we obtain the mean speed $u_{\mathrm{Nof}} = g's/f$. As explained in Wåhlin and Walin [9], the volume of the vein is controlled via the Ekman pumping in the boundary layer, which entrains and detrains water from the friction layer [8,9] and can be written as

$$\partial_t h + \partial_x(uh) + \partial_y(\mathrm{v}h) = -\mathrm{div}(\underline{T}_{\mathrm{Ek}}), \tag{4}$$

where the Ekman pumping is given by [49] $\mathrm{div}(\underline{T}_{\mathrm{Ek}}) = \frac{\delta_{\mathrm{Ek}}}{2}[\partial_x u + \partial_y \mathrm{v} - \zeta]$, where $\delta_{\mathrm{Ek}} = \sqrt{2\nu/f}$ is the thickness of the Ekman layer. Substituting into Eq. (4) leads to

$$\partial_t h + \partial_x\left(u\left[h + \frac{\delta_{\mathrm{Ek}}}{2}\right]\right) + \partial_y\left(\mathrm{v}\left[h + \frac{\delta_{\mathrm{Ek}}}{2}\right]\right) = \frac{\delta_{\mathrm{Ek}}}{2}\zeta. \tag{5}$$

We suppose that the domain is periodic in x as in our experiment. Thus, integrating along slope [Eq. (5)], the flux term $\partial_x(u[h + \frac{\delta_{\mathrm{Ek}}}{2}])$ vanishes. A temporal average of the equation will also suppress the temporal evolution of h for a statistically stationary dynamics. Integrating along y to make appear the across-slope flux, we obtain

$$\left\langle \int \left[\mathrm{v}\left(h + \frac{\delta_{\mathrm{Ek}}}{2}\right)\right]_{y_t}^{y_b} dx \right\rangle_t = \frac{\delta_{\mathrm{Ek}}}{2} \iint \langle \zeta \rangle_t \, dx \, dy. \tag{6}$$

A balance can be established between the incoming flux above the vein Q_{inj} and the transport through the Ekman layer downward [8]. If we consider two locations, the upper one y_t being at the injection and the lower one y_b being at the intrusion level, this balance can be written as

$$Q_{\mathrm{inj}} = \mathrm{v}(y_t)\left[h(y_t) + \frac{\delta_{\mathrm{Ek}}}{2}\right] = \mathrm{v}(y_b)\frac{\delta_{\mathrm{Ek}}}{2}, \tag{7}$$

in which we consider that the vein vanishes before reaching the pycnocline, i.e., $h(y_b) \ll \delta_{\mathrm{Ek}}$. In this case, the spatially averaged Ekman pumping is zero, and so is the averaged vorticity. If there is an overall anomaly of Ekman pumping, this balance is broken and a supplementary down- or up-slope transport through the vein takes place.

A flow with a vanishing average vorticity is the critical state of our system in terms of SOC. In the present experiments, the injection velocity u_j exceeds the geostrophic velocity u_{Nof}, and a negative vorticity anomaly is created in the vein producing Ekman pumping out of the vein. This results in the decrease of the vein height h and a stretching of the upper layer. By conservation of potential vorticity, a barotropic cyclonic vorticity anomaly is created. This phenomena is well documented from observations [20,21] and from laboratory experiments [4–7,19]. The cyclonic vorticity is of the order f [5,19] and competes in the transport balance Eq. (6) with the baroclinic vorticity in the vein of the order $\zeta_0 = u_{\mathrm{Nof}}/L_y$ where L_y is the across-slope extension of the vein. Their ratio ζ_0/f represents a Rossby number which is always below unity in the vein because of the geostrophic equilibrium, implying that the initial anticyclonic anomaly is supplanted by the barotropic cyclonic vorticity of the surface eddies. When this happens, the positive vorticity anomaly in the vein subtracts water from the friction layer and injects it into the vein. To keep the balance given in Eq. (6), this exceeding water is discharged from the vein through the cascading. We can expect that the left-hand side of Eq. (6) scales as the intrusion's transport from cascading

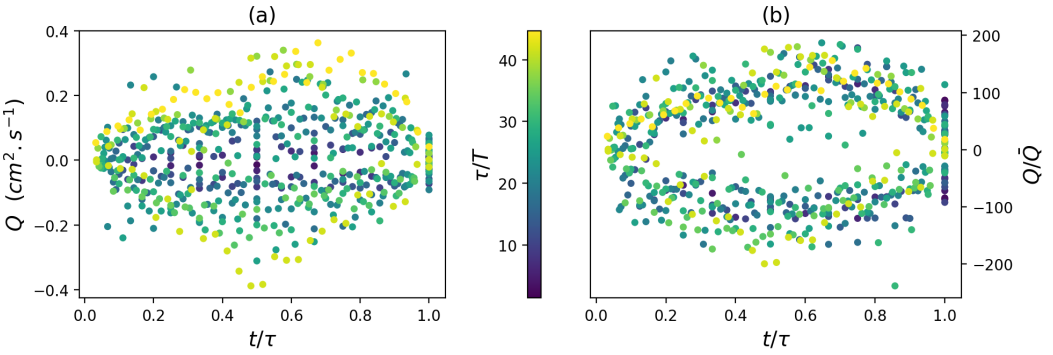

FIG. 8. Dimensional radial transport $Q(t)$ (a) and normalized radial transport $Q(t)/\bar{Q}$ (b) for the lifetime of an intrusion from cascading for Exp05. The colorbar indicates the different lifetime of the intrusions. Values for a given lifetime are averaged over all events with the same lifetime.

$\bar{Q}$ multiplied by the intrusion thickness H and the integrated vorticity in the vein as $u_{\mathrm{Nof}}/L_y\, 2\pi L\, L_y$ where $L = 6\,\mathrm{m}$ gives the horizontal length scale (see Sec. II). Hence

$$H\bar{Q} \propto \frac{\delta_{\mathrm{Ek}}}{2} u_{\mathrm{Nof}} L, \tag{8}$$

where we recall $H = \gamma h_b$ and $\gamma = (\rho_j - \rho_t)/(\rho_b - \rho_t)$ being a ratio of density differences which measures the portion of intruding water in the bottom layer (see Sec. II). We then define the scale for the intrusion's transport by $T_{\mathrm{c}} = (\delta_{\mathrm{Ek}} u_{\mathrm{Nof}}/2)(L/H)$.

Figure 7(b) presents the normalized transport $\bar{Q}/T_{\mathrm{Ek}}$ and the data appear to collapse. This implies that

$$\langle \bar{Q}|\tau \rangle \propto T_{\mathrm{c}} \left(\frac{\tau}{T}\right)^{\beta}, \tag{9}$$

with β around 0.9, obtained by a linear regression of the data in Fig. 7(b).

Figure 8 displays the radial transport $Q(t)$ as a function of time in dimensional form (a) and rescaled with the mean transport $\bar{Q}$ in (b), where a clear collapse of the data is reported. This result additionally supports a SOC behavior, implying autosimilarity without any characteristic length scale [53]. The intrusion of saline water produces vorticity and turbulence in the receiving ambient. This is analyzed in the next section.

IV. EFFECTS OF THE INTRUSION IN THE AMBIENT INTERIOR

A. Vorticity

To better quantify the vorticity in the ambient interior through the intrusion from cascading, we present in Fig. 9 the probability density function (PDF) of the vorticity fields within the area $r < 250\,\mathrm{cm}$ at different times during the experiments Exp06 [Fig. 9(a)], Exp05 [Fig. 9(b)], Exp07 Fig. 9(c)], and Exp09 Fig. 9(d)], to highlight both the influence of the background rotation [$f = 0.105\,\mathrm{s}^{-1}$ (a), $f = 0.21\,\mathrm{s}^{-1}$ (b), $f = 0.14\,\mathrm{s}^{-1}$ (c), (d)] and the intrusion type [$\rho_t < \rho_j < \rho_b$ (a), (b), (c) and $\rho_j = \rho_b > \rho_t$ (d)]. The cyclonic vorticity in the central area $r < 250\,\mathrm{cm}$ in the early stage of the experiment is evident for all cases and is entrained by the positive circulation of the DBC. As discussed in Sec. III A, intrusions from cascading develop cores of negative vorticity close to the slope, and the distributions become bimodal with positive and negative modes. For those experiments in which the intrusion happens at the pycnocline only [Exp06 (a), Exp05 (b), and Exp07 (c)], the negative vorticity peak becomes more pronounced with time [cf. Fig. 9(c)];

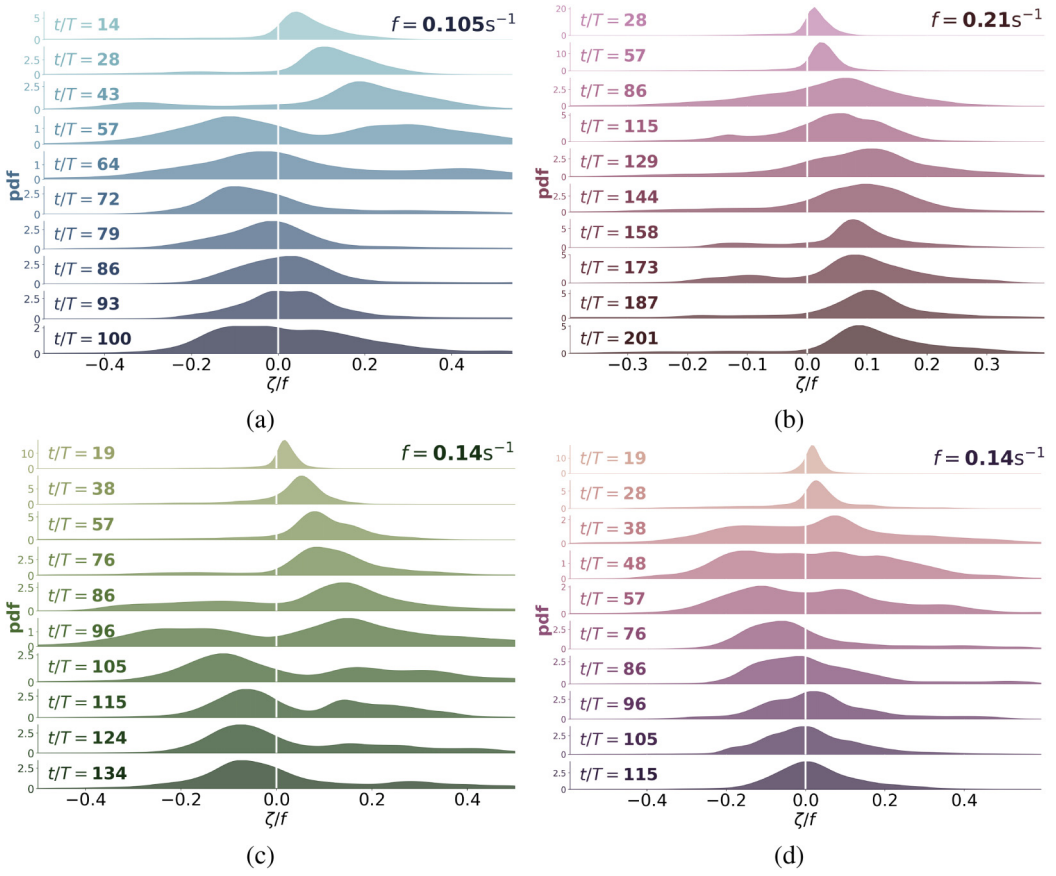

FIG. 9. PDF of vorticity in the ambient interior for $r < 250\,\text{cm}$ and at 10 different times (from top to bottom) for experiments Exp06 (a), Exp05 (b), Exp07 (c), and Exp09 (d).

this is more evident for lower rotation rates [Exp06, Fig. 9(a)]. For strong rotation rates, instead, the intrusion penetrates less resulting in less pronounced peaks of negative vorticity, as given in Fig. 9(b). The positive vorticity peak moves to larger values as a result of the acceleration of the DBC induced by the cascading intrusion (see Sec. III A), adding momentum. In the experiments where the intrusion happens at the pycnocline only, as in Exp07, the vortices generated by the intrusion from cascading are only anticyclonic.

The influence of the injected density relative to the receiving ambient is shown in Figs. 9(c) and 9(d), comparing experiments Exp07 and Exp09, respectively. For the bottom intrusive cases as Exp09, part of the intrusion keeps the contact with the bottom boundary, and friction counteracts the Coriolis force, resulting in the formation of also cyclonic vortices. While the negative mode becomes dominant for Exp07, the distribution is centered for Exp09 with a single mode after approximately $t/T = 80$ [see Fig. 9(d)].

In the experiment Exp07 for $t/T > 120$, cascading events are so intense that they start to deform and break the DBC structure as described already in Sec. III A, which may result in several closed cyclonic loops in the ambient interior as seen in Fig. 10 by the gray contours (see also Fig. 4). These structures can persist several rotational days before merging and transporting negative vorticity into the central part of the tank. For Exp06, which is the longest experiment available, we see that the final breakup of the DBC becomes irreversible: the detached DBC completely disappears, leaving cyclonic loops in the ambient interior.

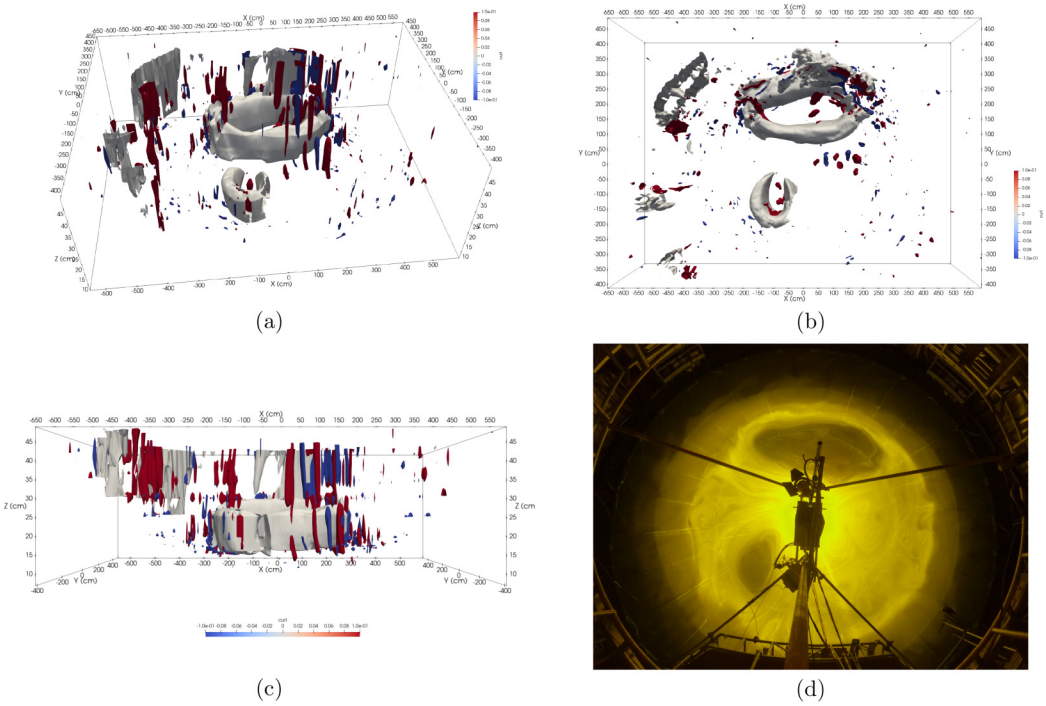

FIG. 10. (a)–(c) 3D visualizations of the vorticity field and speed isosurfaces at $t/T = 125$ for Exp07. The curl isosurfaces are $0.1\,\mathrm{s}^{-1}$ (red) and $-0.1\,\mathrm{s}^{-1}$ (blue). The speed isosurface (in gray) is $2\,\mathrm{cm\,s}^{-1}$. (d) Top view of the experiment recorded by a GOPRO camera. The intruding water is highlighted by the fluorescent dye.

The 3D visualizations of Figs. 10 and 11 also highlight the formation of columnar vortices in the DBC, close to the bottom slope, suggesting that the turbulence generated is mainly two-dimensional, as will be discussed in Sec. IV B further below.

Figures 10 and 11 show that the columnar vortices have the same vertical extension as the intrusion thickness, which is smaller for the experiments with the intrusion at the pycnocline only (e.g., Exp05, Exp06, Exp07, Exp11), forming a third layer of different density, as compared to Exp09 in which the intrusion happens troughout the bottom layer in the receiving ambient (see Fig. 11). Note that the DBC is more pronounced in the experiments in which the intrusion happens at the pycnocline only (e.g., Exp07) as compared to Exp09, where it is weaker but distributed on the full bottom layer extent.

B. Turbulence characteristics

In this section, we evaluate the turbulence characteristics within the ambient interior induced by the gravity current intrusion. Velocities are considered at the pycnocline levels. For the intrusive experiment Exp07, horizontal velocities are computed as a vertical average over six PIV levels around the depth where the vertical density gradient $\partial_z \rho$ is found to be maximum. For Exp09, velocities are computed as a vertical average over the six deeper PIV levels ranging from $z = 7\,\mathrm{cm}$ and $z = 15\,\mathrm{cm}$. The dependence of the results on the definition of the pycnocline height have been tested with no significant changes.

Due to the azimuthal symmetry, we consider azimuthal averages $\langle\cdot\rangle$ and fluctuations $\langle\cdot'\rangle$ At the center of the tank, the presence of the glass cylinder containing the rotating mirror may produce perturbations [19]. For these reasons, the data for $r \leqslant 50\,\mathrm{cm}$ are not considered. Figure 12 displays the instantaneous spatial averaged radial profile of the mean flow (continuous lines) and the RMS

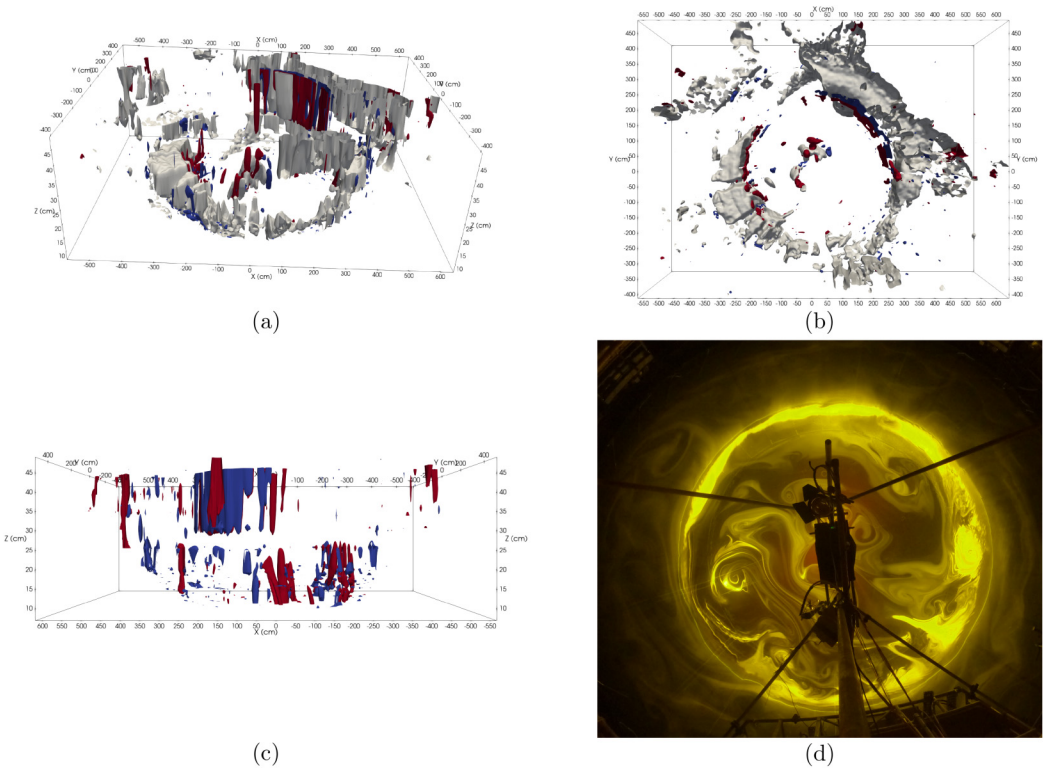

FIG. 11. (a), (b) 3D visualizations of the vorticity field and speed isosurfaces at $t/T = 112$ for Exp09. The curl isosurfaces are $0.1\,\mathrm{s}^{-1}$ (red) and $-0.1\,\mathrm{s}^{-1}$ (blue). The norm velocity isosurface (in gray) is $1.5\,\mathrm{cm\,s}^{-1}$. (c) Same as (a), (b) but without speed isosurfaces. (d) Top view of the experiment recorded by a GoPro camera.

fluctuations (dashed lines) at $t/T = 121$, for Exp07. The flow in the ambient interior is characterized by a mean velocity component which is mainly azimuthal $\langle u_\theta \rangle$ with the largest values for $80\,\mathrm{cm} < r < 200\,\mathrm{cm}$, whereas the radial velocity component has its maximum close to the center for $r \leqslant 100\,\mathrm{cm}$, but being one order of magnitude less than the azimuthal mean component, i.e., $\langle u_r \rangle \ll \langle u_\theta \rangle$. This mean flow is the DBC described previously.

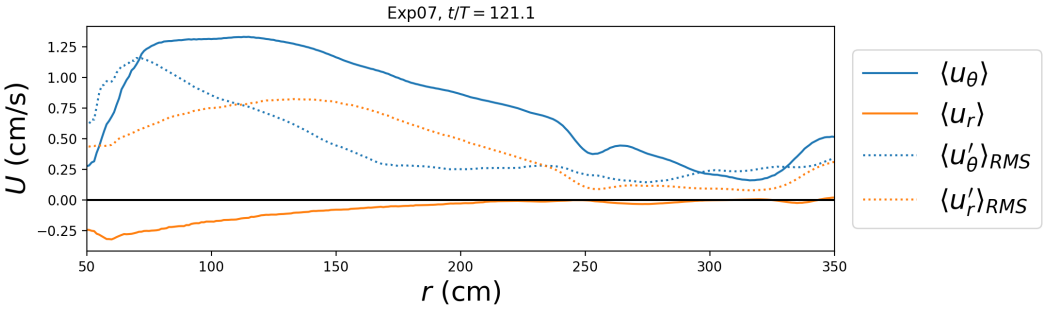

FIG. 12. Instantaneous spatially averaged radial profiles of the mean flow $\langle u_r \rangle$ and $\langle u_\theta \rangle$ (continuous lines) and the RMS fluctuations $\langle u'_\theta \rangle_{RMS}$ and $\langle u'_r \rangle_{RMS}$ (dashed lines) at $t/T = 121$ for Exp07.

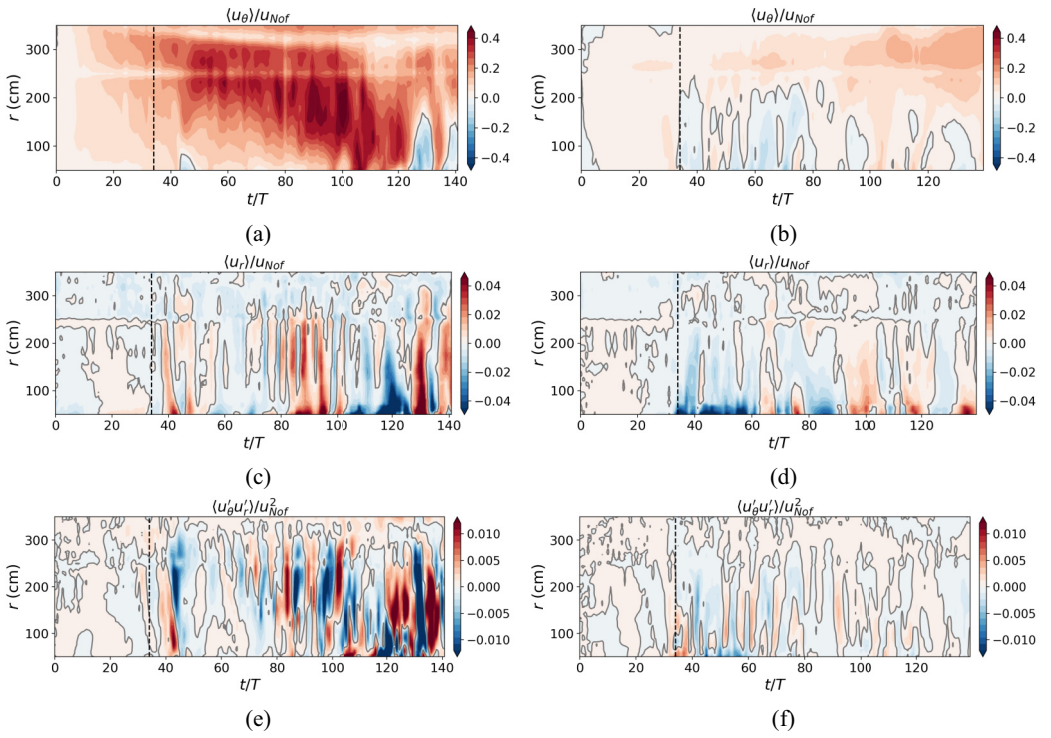

FIG. 13. Hovmöller diagrams of the normalized averaged velocity fields $\langle u_\theta \rangle$ (a), (b), $\langle u_r \rangle$ (c), (d) and the Reynolds stress component $\langle u'_\theta u'_r \rangle$ (e), (f), normalized using the squared Nof speed u^2_{Nof}, for Exp07 (left column) and Exp09 (right column). The vertical dashed lines indicate the time at which the first intrusion in the ambient interior is detected.

Both components of the velocity fluctuations (dashed lines in Fig. 12) are of the same order of magnitude, with values similar to those of the azimuthal mean flow, suggesting horizontal isotropy of the turbulence.

Figure 13 presents Hovmöller diagrams of the normalized averaged velocity fields $\langle u_\theta \rangle$ [(a) and (b)], $\langle u_r \rangle$ [(c) and (d)], and the Reynolds stress component $\langle u'_\theta u'_r \rangle$ [(e) and (f)], normalized using the squared geostrophic velocity u^2_{Nof}, for Exp07 (left column) and Exp09 (right column).

For the intrusive experiment Exp07, the mean flow is dominated by its azimuthal component during the whole experiment, inducing a global cyclonic circulation in the ambient interior. This mean circulation corresponds to the DBC. The DBC is weaker (approximately half) in Exp09 than in Exp07. Also in Exp09, we observe a temporal and spatial variability of the global circulation sign for $r \leqslant 200$ cm. According to the results presented in Fig. 12, the mean radial velocities remain one order of magnitude less than the azimuthal component and do not exhibit a preferential sign. The Reynolds stress, shown in Figs. 13(e) and 13(f), has no preferential sign and is of the order of a few percent of the squared geostrophic velocity u^2_{Nof} starting from the first intrusion (depicted by the vertical dashed line). Values are approximately half for Exp09 with respect to Exp07.

Supposing that the flow is Boussinesq and two-dimensional, the turbulent kinetic energy budget reads

$$[\partial_t + \langle u_r \rangle \partial_r] k = -\frac{1}{\rho_j} \partial_r \langle u'_r p' \rangle - \frac{1}{2} \partial_r \langle u'_r u'^2 \rangle - \langle u'_\theta u'_r \rangle \partial_r \langle u_\theta \rangle - \langle u'^2_r \rangle \partial_r \langle u_r \rangle + \nu \Delta k - \nu \langle d^2 \rangle, \quad (10)$$

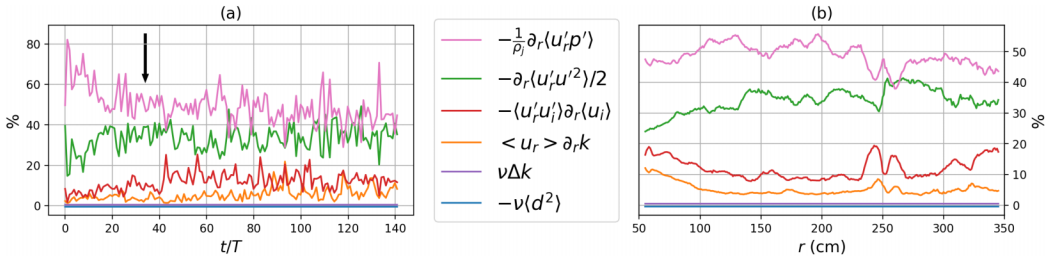

FIG. 14. Relative contribution of the different terms of Eq. (10) with respect to the sum of the absolute value of each contribution, i.e., $|P_j|/\sum_i |P_i|$ for Exp07, averaged over the radial dimension (a) and over time (b). The vertical arrow in (a) marks the first detection of the intrusion in the ambient interior. Note that before this instant k is very low (see top panels of Fig. 15).

where the turbulent kinetic energy k is defined as

$$k = \tfrac{1}{2}\left(\langle u_r'^2\rangle + \langle u_\theta'^2\rangle\right). \tag{11}$$

The term $\partial_t k$ stands for the Eulerian variations of the turbulent kinetic energy. The term $-(1/\rho_j)\partial_r\langle u'_r p'\rangle$ describes the turbulent transport of buoyancy, since $\partial_z p' = \rho' g$ with $\rho = \rho_j + \rho'$. The term $-\partial_r\langle u'_r u'^2/2\rangle$ represents the turbulent energy flux with $u'^2 = u_r'^2 + u_\theta'^2$. The term $-\langle u'_i u'_j\rangle\partial_i\langle u_j\rangle = -\langle u'_\theta u'_r\rangle\partial_r\langle u_\theta\rangle - \langle u_r'^2\rangle\partial_r\langle u_r\rangle$ represents the energy exchange between the mean flow and the fluctuations, while the term $\langle u_r\rangle\partial_r k$ is the radial transport of turbulent kinetic energy. The term $\nu\Delta k$ is the diffusion of turbulent kinetic energy due to viscosity. Finally, $d^2 = \partial_i u'_j \partial_i u'_j$ represents the viscous dissipation. All terms are calculated directly from the PIV velocity data with exception of the turbulent transport of buoyancy $-(1/\rho_j)\partial_r\langle u'_r p'\rangle$, which has been deduced from Eq. (10). This term is correctly predicted if the energy dissipation is well resolved by the PIV measurements. As the flow is two-dimensional, turbulence theory predicts that energy is transferred to large scales, and that dissipation at small scales, represented by the terms $\nu\Delta k$ and $-\nu d^2$, is negligible [49,55]. This will also be confirmed further in Fig. 15. Dissipation is thus correctly measured by the PIV.

Figure 14 plots the relative contribution of the different terms of Eq. (10) with respect to the sum of the absolute value of each contribution, i.e., $|P_j|/\sum_i |P_i|$. These quantities are hence a function of time and the radial position. In order to compare each contribution, the average over the radial dimension and over time are presented in Figs. 14(a) and 14(b), respectively. The dominant terms in the turbulent kinetic energy production appear to be the turbulent transport of buoyancy (pink line, $\approx$50%) and the turbulent energy flux (green line, $\approx$35%). The exchange with the mean flow represents 10% (red line) of the budget, while the radial transport contributes to 5% (orange line). The terms of viscous diffusion (purple line) and viscous dissipation (blue line) are very close to zero. These results demonstrate hence that the turbulence is created by the intrusion, mainly issued by cascading, rather than by the shear of the mean flow.

Since the mean flow component is azimuthal, better represented in polar coordinates, we calculate the energy spectra using second-order structure functions instead of using the Fourier transform, which is designed for Cartesian coordinates. The horizontal isotropy of the turbulent flow allows to consider the second-order transverse horizontal structure function, defined as

$$\langle \delta u^2(l)\rangle = \frac{1}{N(l)}\sum_{\underline{x}}\sum_{||\underline{e}_l||=1}\left([\underline{u}(\underline{x}+l\underline{e}_l) - \underline{u}(\underline{x})]\cdot\underline{e}_l\right)^2, \tag{12}$$

where l is a correlation distance, $\underline{e}_l$ a horizontal unit vector, and $N(l)$ is the number of grid point pairs for a given l. The vectors $\underline{x}$ and $\underline{u}$ are, respectively, the horizontal position and velocity. The second-order structure function is related to the energy spectra $E(\kappa)$, with $\kappa = 1/l$ representing the

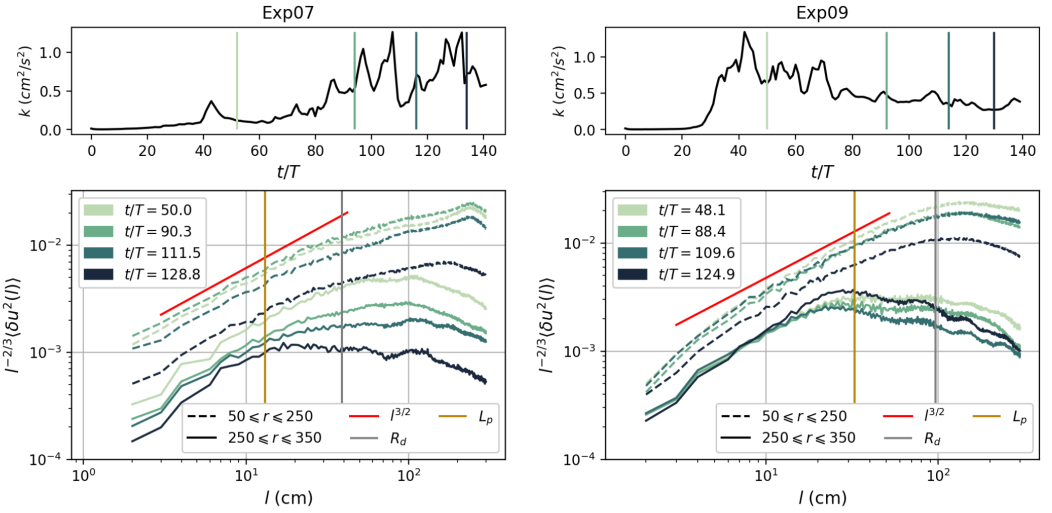

FIG. 15. Top panels: Temporal evolution of the normalized turbulent kinetic energy k; Bottom panels: Second-order transverse structure functions $\langle \delta u^2(l) \rangle$ compensated by a factor $l^{2/3}$ for four different times of Exp07 (a) and Exp09 (b). The vertical lines in the top panels indicate the different times at which the structure functions are computed in the bottom panels. Note that the magnitude of the structure functions computed in the central area (solid lines) have been vertically shifted by a factor 0.3 for illustration purposes. The vertical lines in the bottom panels represent the length scale of the intrusion L_p (yellow) and the Rossby deformation radius $R_d = \sqrt{g'H}/f$ (gray).

wave number, via the relation [56]

$$\langle \delta u^2(l) \rangle \propto l^{-1} E(1/l). \tag{13}$$

Because of the high spatial resolution of the experiment, we used the Monte Carlo method to reduce the calculation time needed for the estimation of the structure functions. The reliability of the results has been tested and the sensitivity analysis is given in the Appendix B. Figure 15 displays the temporal evolution of the turbulent kinetic energy k (top panels) and the second-order transverse structure function $\langle \delta u^2(l) \rangle$, normalized by $l^{2/3}$ of Exp07 (a) and Exp09 (b) (bottom panels). The top panels of Fig. 15 reveal that the turbulent kinetic energy is nonstationary. A first intrusion is observed for Exp07 at $t/T \approx 40$; then an important increase at $t/T \approx 70$ is reported, with large values kept throughout the experimental duration. In Exp09, the first intrusion is detected at $t/T \approx 30$, and then a strong increase is reported with a following small decrease until the end of the experiment. For each experiment, we have chosen four instants highlighted with vertical lines in the top panels of Fig. 15. The dashed lines in the bottom panels of Fig. 15 represent the second-order structure functions within an annulus of 50 cm $\leqslant r \leqslant$ 250 cm (hereafter also referred as central deep area), whereas solid lines represent the structure functions in an annulus 250 cm $\leqslant r \leqslant$ 350 cm. The fact that the structure functions do not exhibit the same shape within these two areas suggests that turbulence is nonhomogeneous.

For both experiments Exp07 and Exp09, the second-order structure functions for 50 cm $\leqslant r \leqslant$ 250 cm exhibit a slope of 3/2 (red solid lines), which would correspond to an energy spectra $E(\kappa) \propto \kappa^{-5/2}$, according to the relation (13). For 250 cm $\leqslant r \leqslant$ 350 cm, the slope of 3/2 is also observed for correlation scales lower than a scale $l \approx \mathcal{O}(10\,\text{cm})$. Note that this scale roughly corresponds to the vertical yellow line, which represents the characteristic length scale of the intrusion L_p. However, at larger scales, slopes are close to 2/3, since they appear horizontal in Fig. 15 for instants of high turbulent kinetic energy, which corresponds to the classical Kolmogorov energy spectra of

slope $-5/3$. The spectra computed in the central area (dashed lines) tend to shift toward larger scales for increasing times, suggesting that energy is also transferred to larger scales, following the classical behavior of 2D turbulence. The gray vertical line represents the Rossby deformation radius R_d, which seems to be less appropriate to characterize the slope change in the bottom panels of Fig. 15 than L_p. No noticeable differences are reported between all the considered experiments having different rotation rates and injection types.

These results demonstrate that the turbulence induced in the ambient interior has a dichotomic behavior. The energy is injected at a scale $\approx L_p$ close to the sloping boundary and forces there the turbulence, whereas, in the central deep area, far from the boundary, the turbulence is forced by the flux from the boundary only, and a freely evolving turbulence dominates with an energy transfer to larger scales.

V. SUMMARY AND CONCLUSIONS

We have presented results from experiments of downslope rotating and intruding gravity currents at high-buoyancy Reynolds numbers, generated using an axisymmetric configuration [19] enabling azimuthal averages. The varied experimental parameters were the rotation rate and the density of the injected saline water with respect to the bottom layer density of the receiving ambient.

Two mechanisms of downward transport of the gravity flow have been identified. The first is the well-known laminar Ekman transport. The incoming buoyancy flux is transported downward through the Ekman layer, which produces a DBC at the intrusion level. This state may be considered as a critical state in terms of SOC. If there is an overall anomaly of Ekman pumping, this balance is broken and a supplementary down- or up-slope transport through the vein takes place. In our experiments, the injection velocity exceeds the geostrophic velocity and a negative vorticity anomaly is created, producing Ekman pumping out of the vein into the Ekman layer. The above water column is stretched, and by conversion of potential vorticity, a barotropic cyclonic vorticity anomaly is generated, competing with the barotropic anticyclonic vorticity from the vein. Hence, the transport balance is perturbed: water is subtracted from the friction layer and injected into the vein. The exceeding water is then discharged downslope from the vein through intermittent and localized events that we call cascading. Both intrusion mechanisms leave a different imprint in the vertical density structure in the ambient interior; this is discussed in Rétif *et al.* [43].

A supplementary effect of the cascading intrusion, is that the DBC generated at the intrusion level from the laminar transport, is deflected, pushed off-shore, and eventually broken. The statistical study of cascading revealed a self-similar internal dynamics, characterized by power-law distributions of their lifetime over more than one decade. The scaled downward transport does not exhibit any characteristic scale, implying that the behavior of the intrusion from cascading is independent from its lifetime. Hence, the dynamics is self-similar, suggesting that the phenomenon is governed by SOC dynamics. These results are also independent of the varied experimental parameters.

Cascading observed in the present study is very different from this described in Shapiro *et al.* [11], which are produced by an external ambient layer flow, or the cascading intended as an overflow from the continental shelf [57]. Here they are produced spontaneously in time and space, without any external tuning, testifying to the intermittent nature of downslope gravity currents in a rotating frame.

Both the intrusions from cascading and the detached DBC are the main contributors to the vorticity production in the ambient interior, in a very different way as compared to previous studies on forced rotating and stratified turbulence [32–34,36–38,44] and closer to realistic ocean configurations. Cascading water brings anticyclonic vorticity, supplementing with the initial cyclonic vorticity generated by the DBC-induced circulation. The vorticity transported into the ambient interior by the intrusion depends on the rotation rate and the intrusion type. Increasing the rotation rate diminishes the penetration distance of intrusions from cascading and thus decreases the input of negative vorticity. For intruding currents over the full bottom layer, friction produces both cyclonic and anticyclonic vorticity, resulting in a balanced distribution between cyclones and anticyclones.

For intrusions propagating within the pycnocline only, anticyclones are dominant. The vertical extension of the vortices is closely related to the penetration thickness and hence is are smaller for the intrusions limited to the pycnocline than for the intrusions propagating through the full bottom layer depth. The top layer also presents columnar vortices, indicating that vorticity is also transmitted to the upper layers through the pycnocline by stretching and compression of the water columns [19].

The turbulence statistics in the ambient interior due to the intrusion reveal to be horizontally isotropic, nonstationary, and nonhomogeneous. After the intrusion has spread, the mean velocity is mainly azimuthal, while the perturbation velocities exhibit the same order of magnitude in both radial and azimuthal directions. The Reynolds stress $\langle u'_\theta u'_r \rangle$ represents 1%–1.5% of the squared geostrophic velocity u^2_{Nof} and are half in magnitude for Exp09, where fluid intrudes over the depth of the bottom layer, as compared to Exp07, where the intrusion is vertically confined to the pycnocline. The transverse structure function distribution computed in the region close to the injection at the sloping boundary and in the central area far from the boundaries reveal different behaviours, with energy injection and energy transfer to larger scales in the former region, and freely evolving turbulence forced at large scales in the latter region.

These results deliver a complementary way to interpret oceanic observations of intrusions from gravity currents in the ocean interior. Their spreading at the neutral buoyancy level is not just issued by shear at the DBC front generated by laminar transport from Ekman dynamics, but is a result of a complex interplay of unstable density fronts, filaments, high-velocity loops originating from detached DBC, and variously sized vortices generated by the intrusion process and their mutual interactions.

Presently, a realistic physical model of the Gibraltar Strait and the Gulf of Cadiz is implemented in the Coriolis Platform (HERCULES experiment). All main forcings are superposed: realistic topography, baroclinic and barotropic forcings, background rotation, and the free surface wind, approaching hence real ocean conditions. In particular, the presence of the tides and the topographic features (i.e. canyons) in this realistic configuration are known to influence the dynamics of the gravity current by modifying the Ekman transport as already shown in Shapiro *et al.* [11] and Darelius and Wåhlin [25]. One of the objectives is to check if the cascading, as observed in the present idealized study, still exists along the Spanish continental shelf presenting a similar circular shape as in the TUBE experiments, despite the increased complexity, using both the new collected experimental data and the observational data of Roustan *et al.* [2].

ACKNOWLEDGMENTS

This work is supported by a grant from the SHOM under contract nr. 20CP03. We are grateful to S. Viboud and T. Valran for their support in conducting the experiments and to J. Sommeria for his support using the UVMAT software. Further thanks go to J. Sommeria, N. Mordant, B. Arrondeau, and S. Rétif for fruitful discussions.

M.E.N. designed and conducted the laboratory experiments. A.W. participated in the design of the experiment. A.T. and M.E.N. processed and analyzed the experimental data. A.T., M.E.N. and A.W. performed the discussion and interpretation of the results and wrote the manuscript.

The authors declare no competing interests.

APPENDIX A: CORRELATION METHOD FOR INTRUSIONS FROM CASCADING

For a chosen radius r considering the radial velocity u_θ as a function of θ, Intrusions from cascading are defined as intervals where the radial velocity u_r at a fixed radius r_{obs} has constant sign. The correlation method used to characterize them relies on the boundaries of these constant-sign intervals. Comparing the length of the interval defined as the intersection between an intrusion from cascading at time t and that at the time $t + \Delta t$, the correlation is built based on the maximum overlap length between the two times. Moreover, the frame at time step t is shifted by the advective angular

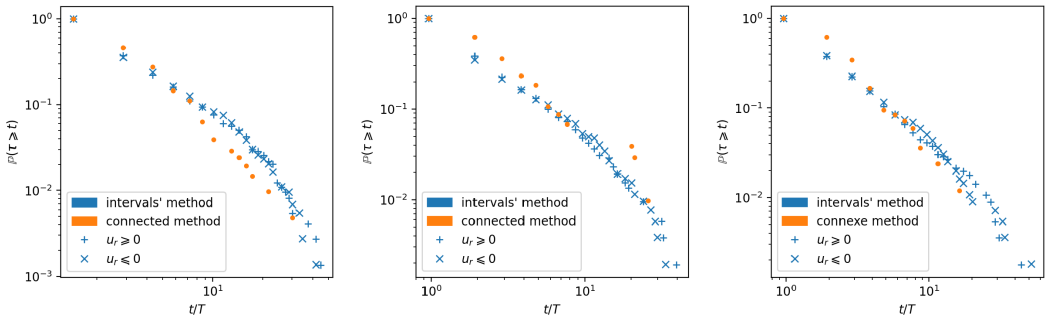

(a) (b) (c)

FIG. 16. Comparison of the different correlation methods for Exp05 (a), Exp07 (b), and Exp09 (c).

velocity $\Omega = u_\theta(t, r, \theta)/r$ such that

$$u_r(t + dt, \theta) \simeq u_r(t, \theta - \Omega dt). \tag{A1}$$

The correlation function is then maximized for each event at time t to be correlated to the events at $t + \Delta t$. Those events that have not been correlated at $t + dt$, are considered as new. The maximum lifetime is found when a zero correlation is found.

If we denote C_i^t the ith interval of constant sign, for example, positive, at time t, with $\theta_i^t \leqslant \theta_{i+1}^t$ the interval's boundaries, the function to maximize in order to correlate the cascading events is as follows:

$$d\left(C_i^{t+\Delta t}, C_j^t\right) = \min\left(\theta_{i+1}^{t+dt}, \theta_{j+1}^t + \Omega\right) - \max\left(\theta_i^{t+dt}, \theta_j^t + \Omega\right). \tag{A2}$$

The development of a correlation algorithm rise some complex questions, in particular about how considering merging intrusions from cascading. In order to test our method of correlation, we compare it with a second one, which we call the connected method. The Hovmöller diagram of Fig. 5 can be transformed into a binary image considering the sign of the velocity field. In this image it is then possible to compute the length, in the temporal dimension, of all the image connected parts with a positive radial velocities. This method is not fully reliable since the periodicity along θ of the image is not taken into account and considers merged intrusions as a single intrusion. However, it also gives an idea of the distribution of the event's lifetime that can be compared with the results obtained with the method described above. The shape of the distribution being similar between the two computation methods, we can be confident of the reliability of the computed correlation as given in Fig. 16.

APPENDIX B: COMPUTATION OF STRUCTURE FUNCTIONS USING THE MONTE CARLO METHOD

PIV fields give access to the velocity in the central area ($r \leqslant 350$ cm) in a grid of typically $N = 10^5$ points. Computing structure function would thus require evaluating velocity differences from $N(N-1)/2 \approx 10^{10}$ pairs. To reduce the computation time, we choose to evaluate structure functions using the Monte Carlo method. We selected randomly a subset of 10^5 pairs and computed the structure functions on these pairs. This operation was repeated 10 times, giving access to an estimate of the variance of this method. The average of these 10 Monte Carlo integration was used as the final estimate of the structure functions and are presented in Fig. 15. Figure 17 presents the variability of the Monte Carlo method. The second-order structure function is calculated for a velocity field at $t/T = 109.6$ and $z = 13$ cm for Exp09. The solid blue line represents the mean of the 10 integrations, and the colored area represents the values between the 0.1 and 0.9 quantiles.

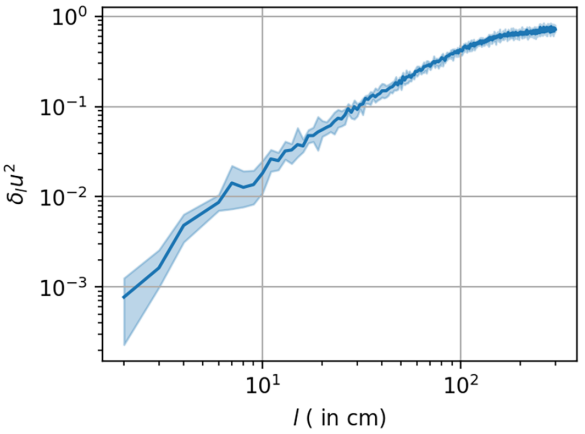

FIG. 17. Monte Carlo variability for the computation of second order transverse structure functions for Exp09, at $t/T = 109$ and at $z = 13$ cm. The solid line represents the averaged value with the shaded area being the 0.1–0.9 quantile.

The variability appears to be of the order of 10^{-3}, and hence, the shape of the structure function is accurately represented by this method.

[1] J. Marschall and F. Schott, Open–ocean convection: Observations, theory, and models, Rev. Geophys. **37**, 1 (1999).
[2] J.-B. Roustan, L. Bordois, F. Dumas, F. Auclair, and X. Carton, In situ observations of the small-scale dynamics at Camarinal Sill—Strait of Gibraltar, J. Geophys. Res.: Oceans **128**, e2023JC019738 (2023).
[3] D. Nof, The translation of isolated cold eddies on a sloping bottom, Deep Sea Res. **30**, 171 (1983).
[4] C. Cenedese, J. Whitehead, T. Ascarelli, and M. Ohiwa, A dense current flowing down a sloping bottom in a rotating fluid, J. Phys. Oceanogr. **34**, 188 (2004).
[5] G. F. Lane-Serff and P. G. Baines, Eddy formation by dense flows on slopes in a rotating fluid, J. Fluid Mech. **363**, 229 (1998).
[6] G. F. Lane-Serff and P. G. Baines, Eddy formation by overflows in stratified water, J. Phys. Oceanogr. **30**, 327 (2000).
[7] D. Etling, F. Gelhardt, U. Schrader, F. Brennecke, G. Kühn, G. Chabert d'Hieres, and H. Didelle, Experiments with density currents on a sloping bottom in a rotating fluid, Dyn. Atm. Oceans **31**, 139 (2000).
[8] A. Wirth, On the basic structure of oceanic gravity currents, Ocena Dyn. **59**, 551 (2009).
[9] A. Wåhlin and G. Walin, Downward migration of dense bottom currents, Env. Fluid Mech. **1**, 257 (2001).
[10] G. Shapiro and A. Hill, Dynamics of dense water cascades at the shelf edge, J. Phys. Oceanogr. **27**, 2381 (1997).
[11] G. I. Shapiro, J. M. Huthnance, and V. V. Ivanov, Dense water cascading off the continental shelf, J. Geophys. Res.: Oceans **108**, 2002JC001610 (2003).
[12] B. Sutherland, J. Nault, K. Yewchuk, and G. Swaters, Rotating dense currents on a slope. Part 1. Stability, J. Fluid Mech. **508**, 241 (2004).
[13] J. Whitehead, Rotating gravity currents, in *Encyclopedia of Ocean Sciences*, 3rd ed., edited by J. K. Cochran, H. J. Bokuniewicz, and P. L. Yager (Elsevier, Oxford, 2019), Vol. 3, pp. 40–44.
[14] K. Speer, E. Tzipperman, and Y. Feliks, Topography and grounding in a simple bottom layer model, J. Geophys. Res.: Oceans **98**, 8547 (1993).

[15] A. Gill, Circulation and bottom water production in the Weddell Sea, Deep Sea Res. Oceanogr. Abstracts **20**, 111 (1973).
[16] P. Emms, Streamtube models of gravity currents in the ocean, Deep Sea Res. **44**, 1575 (1997).
[17] J. Price and M. O'Neil Baringer, Outflows and deep water production by marginal seas, Prog. Oceanogr. **33**, 161 (1994).
[18] C. Cenedese and C. Adduce, A new parameterization for entrainment in overflows, J. Phys. Ocean. **40**, 1835 (2010).
[19] M. E. Negretti, F. L. Tucciarone, and A. Wirth, Intruding gravity currents and re-circulation in a rotating frame: Laboratory experiments, Phys. Fluids **33**, 096607 (2021).
[20] J. Bruce, Eddies southwest of the Denmark Strait, Deep Sea Res. **42**, 13 (1995).
[21] W. Krauss, A note on overflow eddies, Deep Sea Res. **43**, 1661 (1996).
[22] P. Richardson, M. McCartney, and C. Maillard, A search for meddies in historical data, Dyn. Atmos. Oceans **15**, 241 (1991).
[23] M. Ungarish, On the spinup and spreadout of a Cartesian gravity current on a slope in a rotating system, J. Fluid Mech. **943**, A31 (2022).
[24] A. Wåhlin, Topographic steering of dense currents with application to submarine canyons, Deep Sea Res. **49**, 305 (2002).
[25] E. Darelius and A. Wåhlin, Downward flow of dense water leaning on a submarine ridge, Deep Sea Res. **54**, 1173 (2007).
[26] A. Wirth and M. E. Negretti, Intruding gravity currents and their recirculation in a rotating frame: Numerical results, Ocean Model. **173**, 101994 (2022).
[27] M. Wells, C. Cenedese, and C. Caulfield, The relationship between flux coefficient and entrainment ratio in density currents, J. Phys. Ocean. **40**, 2713 (2010).
[28] R. Ferrari and P. Wunsch, Ocean circulation kinetic energy: Reservoirs, sources, and sinks, Annu. Rev. Fluid Mech. **41**, 253 (2009).
[29] R. Ferrari, A. Mashayek, and T. J. McDougall, Turning ocean mixing upside down, J. Phys. Ocean. **46**, 2239 (2016).
[30] R. McDougall and R. Ferrari, Abyssal upwelling and downwelling driven by near-boundary mixing, J. Phys. Ocean. **47**, 261 (2017).
[31] A. Rubino, M. Gacic, M. Bensi, V. Kovacevic, V. Malacic, M. Menna, M. E. Negretti, J. Sommeria, D. Zanchettin, R. V. Barreto *et al.*, Experimental evidence of long-term oceanic circulation reversals without wind influence in the north Ionian Sea. Sci. Rep. **10**, 1905 (2020).
[32] E. Hopfinger, F. Browand, and Y. Gagne, Turbulence and waves in a rotating tank, J. Fluid Mech. **125**, 505 (1982).
[33] E. C. Itsweire, K. N. Helland, and C. W. Van Atta, The evolution of grid-generated turbulence in a stably stratified fluid, J. Fluid Mech. **162**, 299 (1986).
[34] K. Yoon and Z. Warhaft, The evolution of grid-generated turbulence under conditions of stable thermal stratification, J. Fluid Mech. **215**, 601 (1990).
[35] S. Narimousa, T. Maxworthy, and G. R. Spedding, Experiments on the structure and dynamics of forced, quasi-two-dimensional turbulence, J. Fluid Mech. **223**, 113 (1991).
[36] P. Linden, B. Boubnov, and S. Dalziel, Source-sink turbulence in a rotating stratified fluid, J. Fluid Mech. **298**, 81 (1995).
[37] A. Fincham, T. Maxworthy, and G. Spedding, Energy dissipation and vortex structure in freely decaying sratified grid turbulence, Dyn. Atm. Oceans **23**, 155 (1996).
[38] O. Praud, A. Fincham, and J. Sommeria, Decaying grid turbulence in a strongly stratified fluid, J. Fluid Mech. **522**, 1 (2005).
[39] E. Lindborg, The energy cascade in a strongly stratified fluid, J. Fluid Mech. **550**, 207 (2006).
[40] J. Riley and S. M. DeBruynKops, Dynamics of turbulence strongly influenced by buoyancy, Phys. Fluids **15**, 2047 (2003).
[41] M. Waite and P. Bartello, Stratified turbulence dominated by vortical motion, J. Fluid Mech. **517**, 281 (2004).

[42] M. Spall, Dynamics of downwelling in an eddy-resolving convective basin, J. Phys. Ocean. **40**, 2341 (2010).
[43] S. Rétif, M. Negretti, and A. Wirth, Unveiling the dynamics of turbulent and laminar intrusions from oceanic gravity current: Insight from large scale laboratory experiment, Sci. Rep. **14**, 10274 (2024).
[44] P. Augier, P. Billant, M. Negretti, and J.-M. Chomaz, Experimental study of stratified turbulence forced with columnar dipoles, Phys. Fluids **26**, 046603 (2014).
[45] P. Augier, P. Billant, and J.-M. Chomaz, Stratified turbulence forced with columnar dipoles: Numerical study, J. Fluid Mech. **769**, 403 (2015).
[46] N. Laanaia, A. Wirth, J.-M. Molines, B. Barnier, and J. Verron, On the numerical resolution of the bottom layer in simulations of oceanic gravity currents, Ocean Sci. **6**, 563 (2010).
[47] C. Vic, G. Roullet, X. Capet, X. Carton, M. Molemaker, and J. Gula, Eddy topography interactions and the fate of the Persian Gulf Outflow, J. Geophys. Res.: Oceans **120**, 6700 (2015).
[48] J. Gula, M. J. Molemaker, and J. C. McWilliams, Topographic generation of submesoscale centrifugal instability and energy dissipation, Nat. Commun. **7**, 12811 (2016).
[49] G. K. Vallis, *Atmospheric and Oceanic Fluid Dynamics* (Cambridge University Press, Cambridge, 2017).
[50] P. Bak, C. Tang, and K. Wiesenfeld, Self-organized criticality, Phys. Rev. A **38**, 364 (1988).
[51] W. Smyth, J. Nash, and J. Moum, Self-organized criticality in geophysical turbulence, Sci. Rep. **9**, 3747 (2019).
[52] D. L. Turcotte, Self-organized criticality, Rep. Prog. Phys. **62**, 1377 (1999).
[53] S. Poincloux, Élasticité et tremblements du tricot, Ph.D. thesis, Physique Sorbonne Universit, 2018.
[54] H. Salehipour, W. Peltier, and C. Caulfield, Self-organized criticality of turbulence in strongly stratified mixing layers, J. Fluid Mech. **856**, 228 (2018).
[55] G. Boffetta and R. E. Ecke, Two-dimensional turbulence, Annu. Rev. Fluid Mech. **44**, 427 (2012).
[56] A. Babiano, C. Basdevant, and R. Sadourny, Structure functions and dispersion laws in two-dimensional turbulence, J. Atmos. Sci. **42**, 941 (1985).
[57] V. Ivanov, G. Shapiro, J. Huthnance, D. Aleynik, and P. Golovin, Cascades of dense water around the world ocean, Prog. Oceanogr. **60**, 47 (2004).